The Astrophysical Journal Letters, 965:L15 (9pp), 2024 April 20 https://doi.org/10.3847/2041-8213/ad3619

Vortex Fiber Nulling for Exoplanet Observations: First Direct Detection of M Dwarf Companions around HIP 21543, HIP 94666, and HIP 50319

Daniel Echeverri[1], Jerry W. Xuan[1], John D. Monnier[2], Jacques-Robert Delorme[3], Jason J. Wang[4], Nemanja Jovanovic[1], Katelyn Horstman[1], Garreth Ruane[5], Bertrand Mennesson[5], Eugene Serabyn[5], Dimitri Mawet[1,5], J. Kent Wallace[5], Sofia Hillman[6], Ashley Baker[1], Randall Bartos[5], Benjamin Calvin[7], Sylvain Cetre[3], Greg Doppmann[3], Luke Finnerty[7], Michael P. Fitzgerald[7], Chih-Chun Hsu[4], Joshua Liberman[8], Ronald López[7], Maxwell Millar-Blanchaer[6], Evan Morris[9], Jacklyn Pezzato[1], Jean-Baptiste Ruffio[10], Ben Sappey[10], Tobias Schofield[1], Andrew J. Skemer[9], Ji Wang[11], Yinzi Xin[1], Narsireddy Anugu[12], Sorabh Chhabra[13], Noura Ibrahim[2], Stefan Kraus[13], Gail H. Schaefer[12], and Cyprien Lanthermann[12]
[1] Department of Astronomy, California Institute of Technology, Pasadena, CA 91125, USA; dechever@caltech.edu
[2] Astronomy Department, University of Michigan, Ann Arbor, MI 48109, USA
[3] W. M. Keck Observatory, 65-1120 Mamalahoa Hwy, Kamuela, HI, USA
[4] Center for Interdisciplinary Exploration and Research in Astrophysics (CIERA) and Department of Physics and Astronomy, Northwestern University, Evanston, IL 60208, USA
[5] Jet Propulsion Laboratory, California Institute of Technology, 4800 Oak Grove Dr., Pasadena, CA 91109, USA
[6] Department of Physics, University of California, Santa Barbara, CA 93106, USA
[7] Department of Physics & Astronomy, 430 Portola Plaza, University of California, Los Angeles, CA 90095, USA
[8] James C. Wyant College of Optical Sciences, University of Arizona, Meinel Building 1630 E. University Blvd., Tucson, AZ 85721, USA
[9] Department of Astronomy & Astrophysics, University of California, Santa Cruz, CA 95064, USA
[10] Department of Astronomy and Astrophysics, University of California, San Diego, La Jolla, CA 92093, USA
[11] Department of Astronomy, The Ohio State University, Columbus, OH 43210, USA
[12] The CHARA Array of Georgia State University, Mount Wilson Observatory, Mount Wilson, CA 91023, USA
[13] School of Physics and Astronomy, University of Exeter, Exeter, EX4 4QL, UK
Received 2023 November 24; revised 2024 February 29; accepted 2024 March 20; published 2024 April 10

Abstract

Vortex fiber nulling (VFN) is a technique for detecting and characterizing faint companions at small separations from their host star. A near-infrared (∼2.3 μm) VFN demonstrator mode was deployed on the Keck Planet Imager and Characterizer (KPIC) instrument at the Keck Observatory and presented earlier. In this Letter, we present the first VFN companion detections. Three targets, HIP 21543 Ab, HIP 94666 Ab, and HIP 50319 B, were detected with host–companion flux ratios between 70 and 430 at and within one diffraction beamwidth (λ/D). We complement the spectra from KPIC VFN with flux ratio and position measurements from the CHARA Array to validate the VFN results and provide a more complete characterization of the targets. This Letter reports the first direct detection of these three M dwarf companions, yielding their first spectra and flux ratios. Our observations provide measurements of bulk properties such as effective temperatures, radial velocities, and $v \sin i$, and verify the accuracy of the published orbits. These detections corroborate earlier predictions of the KPIC VFN performance, demonstrating that the instrument mode is ready for science observations.

Unified Astronomy Thesaurus concepts: Exoplanet detection methods (489); Astronomical instrumentation (799); Direct detection interferometry (386); High resolution spectroscopy (2096); Companion stars (291)

1. Introduction

Decades of radial velocity (RV) surveys have revealed that giant planets are most likely to orbit between 1 and 10 au from their host stars (Fulton et al. 2021; Rosenthal et al. 2021). However, typical coronagraphs have inner working angles (IWA) of about 3 λ/D (Macintosh et al. 2014; Beuzit et al. 2019), so they cannot efficiently observe exoplanets at small separations. Here, λ is the operating wavelength and D is the telescope diameter, such that 3 λ/D at 2.3 μm on a 10 m telescope corresponds to 14 au for a star at 100 pc. This puts the bulk of the giant planet population inside the IWA in the near-infrared, and limits the spectral coverage of direct imagers for planets close to their star. Interferometric techniques can nevertheless access smaller separations and therefore provide the best opportunity for detecting giant planets in the near-infrared.

Vortex fiber nulling (VFN) is a single-aperture interferometric technique for detecting and characterizing faint companions at small separations (Ruane et al. 2018; Echeverri et al. 2019; Ruane et al. 2019; Echeverri et al. 2021). VFN uses an optical vortex mask (Beijersbergen et al. 1994) to impart a phase pattern that, when centered on a single-mode fiber, is orthogonal to the fiber's fundamental mode. Thus, a star can be aligned on-axis so that its light is rejected by the fiber while off-axis planet light couples in and is routed to a spectrograph for characterization. VFN's simple optical design makes it easy to implement on existing and upcoming high-contrast imaging instruments with a fiber injection unit, thereby providing access to companions at $\lesssim 1\ \lambda/D$ ($\lesssim$5 au at 100 pc for $\lambda = 2.3\ \mu$m and $D = 10$ m). An on-sky VFN demonstrator is now operational (Echeverri et al. 2023) as a new mode in the Keck Planet Imager and Characterizer (KPIC; Mawet 2021; Delorme et al. 2021; Echeverri et al. 2022; N. Jovanovic et al. 2024, in preparation) instrument at the Keck II

Telescope. The nominal KPIC observing mode, referred to as direct spectroscopy (DS) since it aligns the fiber directly to the desired target, does not use a coronagraph and provides $R \sim 35{,}000$ spectra that have been used extensively to spectroscopically characterize exoplanets and brown dwarf companions (Wang et al. 2021, 2022, 2023; Ruffio et al. 2023; Delorme et al. 2021; Xuan et al. 2022; Finnerty et al. 2023). The new KPIC VFN mode builds on this to provide similar spectra for characterization at smaller separations. Additionally, since the VFN mode does not require prior knowledge of the exact position of the companion, it can be used to detect new companions. Previous commissioning results showed that ignoring systematics such as fringing, the KPIC VFN mode's on-sky performance is sufficient for detecting companions 1000 times fainter than their host in the K band (2.0–2.4 μm) in 1 hr at separations of 30–80 mas (Echeverri et al. 2023).

In this Letter, we now present the first detections from this new demonstrator mode. The three companions covered here were previously known only from RV and/or astrometric observations, such that our results represent their first direct detections and provide the first spectra for the companions. Though KPIC VFN alone can provide a detection, in this Letter we complement the VFN observations with CHARA observations using the MIRC-X and MYSTIC beam combiners (Anugu et al. 2020; Setterholm et al. 2023), which have a demonstrated history of success at these angular separations (e.g., Roettenbacher et al. 2015a, 2015b; Thomas et al. 2021; De Furio et al. 2022; Lanthermann et al. 2023). This allows us to validate the VFN performance in this first demonstration against CHARA's well-established performance. For example, the CHARA data ensured that the published orbital parameters were well enough constrained that the targets were indeed within the current VFN field of view (~30–80 mas) at the time of observation. Like this, if there were a VFN nondetection or anomalous result, we could be certain it was not due to the companion being too faint or beyond the VFN field of view. Moreover, the CHARA data provides complementary information to the VFN spectra. The latter cannot constrain the companion position nor flux ratio, as the two parameters are degenerate in VFN's single annular coupling region. Thus, the CHARA results provide the first flux ratio measurements for the companions, highlighting some of the synergies between these long-baseline interferometry and vortex fiber nulling techniques.

2. Targets

We targeted three nearby G stars with known companions at small separations. Table 1 lists the targets and basic parameters of the primary star while the remainder of this section provides previously known details on each target.

HIP 21543 (HD 29310, vB 102) is a triple system in the Hyades cluster with an inner single-lined spectroscopic binary (SB1) first detected by Griffin et al. (1988) and an outer visual companion originally detected at 0.″25 by Mason et al. (1993). The inner SB1 is the target of this Letter. Tokovinin (2021) combines RV observations with measurements of the astrometric wobble of the outer companion (referred to as B) to provide a refined orbit for both the inner (referred to as Aa,Ab) and outer components. This puts Ab on a 734 ± 0.3 yr orbit with a 37 mas semimajor axis, and B on a 125 yr orbit with a 670 mas semimajor axis. The mass ratio for Aa,Ab from their orbits is 0.29 such that given the estimated mass for Aa of 1.13 $M_\odot$, Ab is about 0.32 $M_\odot$. Bender & Simon (2008) reported weak lines from Ab, which would make this a double-lined spectroscopic binary with a direct detection, but Tokovinin (2021) found that the measured RVs for the Ab lines are inconsistent with the astrometric wobble measurements. We note that the Tokovinin (2021) orbits show Ab and B counterorbiting around the central Aa star, implying an unusual orbital architecture for the system.

An orbit for the inner Aa,Ab component is also reported in the Gaia DR3 nonsingle star (NSS) solutions (Gaia Collaboration et al. 2023; Holl et al. 2023). The listed orbital period is 739 ± 7 days, consistent with the Tokovinin (2021) value. From isochrone fitting, Gaia estimates the mass of Aa at $1.01 \pm 0.06\ M_\odot$, which allows them to predict the mass of Ab at $0.21 \pm 0.03\ M_\odot$ (see Gaia DR3 `binary_masses` table; Gaia Collaboration et al. 2023). With the Gaia-derived masses, we roughly estimate the ΔK mag between Aa and Ab. For Aa, we use the Two Micron All Sky Survey (2MASS) K magnitude assuming it is dominated by the brighter primary star and neglecting its variability as a BY Draconis variable since the V-band variability amplitude is only 0.03 mag (Lockwood et al. 1984), and likely even less in the K band. Thus, we estimate an absolute magnitude $M_K = 2.77$ given the Gaia parallax of 22.69 mas for the distance. For Ab, we use the latest version of the main-sequence dwarf table (MSDT) by Pecaut & Mamajek (2013) to estimate $M_K \approx 7.6$ assuming 0.21 $M_\odot$. This gives $\Delta K \sim 4.83$ for a flux ratio of ~85 between the stars. A similar procedure but using the Tokovinin masses yields $\Delta K \sim 4.06$ (flux ratio ~40).

HIP 94666 (HD 180683) is also a triple system. There is an inner SB1 (Aa,Ab) with an orbital period of 1210 days provided by Tokovinin (2018). The outer visual companion, B, is on a ~3000 yr orbit at 3.6″ (Riddle et al. 2015; Roberts et al. 2017). Though a full orbital solution is not provided in these prior works, the Gaia DR3 NSS table has a solution with a period of 1211 ± 29 days that is consistent with the published period for Aa,Ab. Gaia did not spectroscopically detect this system, so the `binary_masses` table only provides a mass for Aa, $1.11^{+0.06}_{-0.10}\ M_\odot$. However, given the primary mass, we can solve for the mass ratio, q, between Ab/Aa using the Thiele–Innes orbital elements from the Gaia DR3 NSS. We obtain $q \approx 0.22$, which yields ~0.24 $M_\odot$ for Ab. We estimate the flux ratio as done for HIP 21543; the 2MASS K magnitude yields an absolute $M_K = 2.23$ for Aa given the 15.52 mas Gaia parallax and the MSDT yields $M_K \approx 7.3$ for Ab. We thus predict $\Delta K \sim 5.07$ (flux ratio ~105).

HIP 50319 (HD 89010, 35 Leo) is an SB1 binary (A,B) with an orbital period of ~537 days (Tokovinin 2014). The Gaia NSS table again provides a full orbital solution, with a period of 524 ± 6 days. The `binary_masses` table does not provide a mass for either star so we use the Tokovinin (2014) mass of ~1.34 $M_\odot$ for A and the Gaia orbit to determine a mass ratio $q \approx 0.11$, and hence a mass for B of ~0.15 $M_\odot$. As done for the other two targets, the 2MASS K magnitude gives an absolute $M_K = 1.88$ for A given the 32.09 mas Gaia parallax. From the MSDT, $M_K \approx 8.4$ for B, so we estimate $\Delta K \sim 6.52$ (flux ratio ~405).

3. Observations and Data Analysis

We observed all three targets with both KPIC VFN and CHARA MIRC-X/MYSTIC. VFN provides high-resolution spectra while CHARA gives the astrometry and flux ratio. Note that the VFN spectra alone provide a detection, but for this first

Table 1
Targets and Observations

Target (HIP) (1)	App. Mag. (K band) (2)	Spec. Type (3)	Dist. (pc) (4)	Pred. Flux Ratio (K) (5)	Date Observed (UT) (6)	Instrument/Mode (7)	Obs. Band (8)	Spectral Resol. (9)	Int. Time (min) (10)	Pred. Sep. (mas;AU[; λ/D][a]) (11)	Pred. RV (km s^{-1}) (12)	Bary. RV (km s^{-1}) (13)
21543	5.992	G0	44.1	40-85	2022 Oct 12	KPIC/VFN	K	35,000	36[b]	48.7;2.1;1.0	−7.9	22.8
21543	5.992	G0	44.1	40-85	2021 Oct 22	CHARA/MIRC-X	H	50	10	20.5;0.9	…	…
21543	5.992	G0	44.1	40-85	2021 Oct 22	CHARA/MYSTIC	K	50	10	20.5;0.9	…	…
21543	5.992	G0	44.1	40-85	2022 Sep 22	CHARA/MIRC-X	H	50	28	47.3;2.1	…	…
21543	5.992	G0	44.1	40-85	2022 Sep 22	CHARA/MYSTIC	K	100	28	47.3;2.1	…	…
94666	6.280	G0	64.4	105	2023 May 09	KPIC/VFN	K	35,000	48	37.3;2.4;0.8	13.5	14.1
94666	6.280	G0	64.4	105	2023 May 15	CHARA/MIRC-X	H	50	9	38.1;2.5	…	…
94666	6.280	G0	64.4	105	2023 May 15	CHARA/MYSTIC	K	100	9	38.1;2.5	…	…
50319	4.345	G0	31.2	405	2023 May 06	KPIC/VFN	K	35,000	123	48.7;1.5;1.0	−9.2	−28.3
50319	4.345	G0	31.2	405	2023 May 23	CHARA/MIRC-X	H	50	46	41.9;1.3	…	…
50319	4.345	G0	31.2	405	2023 May 23	CHARA/MYSTIC	K	50	46	41.9;1.3	…	…
50319	4.345	G0	31.2	405	2023 May 24	CHARA/MIRC-X	H	50	37	41.5;1.3	…	…
50319	4.345	G0	31.2	405	2023 May 24	CHARA/MYSTIC	K	50	37	41.5;1.3	…	…

Notes. The first column is the Hipparcos number for the target. Second is the apparent K-band magnitude from the Two Micron All Sky Survey Catalog. The spectral type is from the Henry Draper Catalog and Extension. The distance, in parsecs, is derived from the parallax in the Gaia DR3 NSS table. The predicted K-band star-to-planet flux ratio is computed and explained in Section 2. Columns (6) through (9) provide the UT date of the observation, the instrument and observing mode, the astronomical band for the mode, and the corresponding spectral resolution ($R = \lambda/\Delta\lambda$). Integration times in column (10) do not include calibrators, only the on-source time integrating for the companion. The predicted separation and RV at the time of observation use the Gaia NSS orbital solutions, except for HIP 21543 for which the Tokovinin (2021) orbit was used. Pred. RV is the relative value between the primary and companion, and is only provided for the VFN data since CHARA cannot measure it. The final column is the average Earth barycentric RV over the observation, and is computed with the `Astropy` Python package. This value is used to translate our measured RVs later in the Letter from the instrument frame to the Earth–Sun barycenter so that values are reported with respect to that barycenter.

[a] λ/D only provided for VFN observations, assuming $\lambda = 2.3$ μm and $D = 10$ m.

[b] Observations were made on two fibers, with 36 minutes per fiber. Only one fiber was used for the analysis.

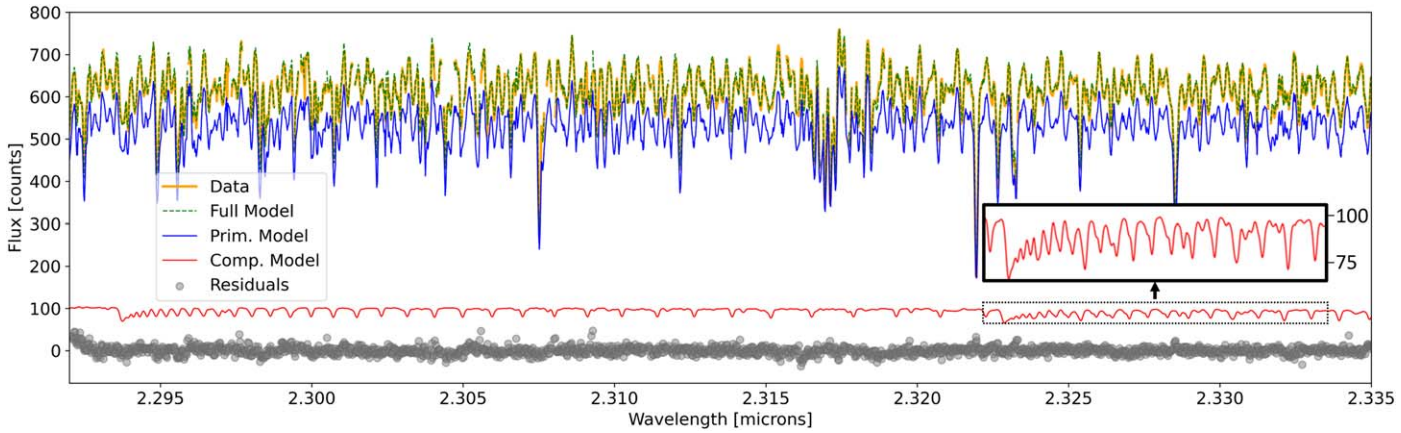

Figure 1. Spectrum at $R \sim 35{,}000$ from VFN observations of HIP 21543. Only KPIC echelle order 6, the one used for the forward model fits, is shown. The raw spectrum has been median-filtered to remove the continuum and is shown as the solid gold line, while the best-fit full model is in dashed green. Various components of the best-fit model are also shown: primary star spectrum (blue), companion spectrum (red), and residuals (gray dots). The companion spectrum is about 5 times fainter than that of the primary after partial nulling of the latter by VFN. The true flux ratio for the system is 70 ± 11, as measured by CHARA and shown in Table 3.

demonstration, we complement the VFN results with CHARA observations to validate the VFN performance and highlight synergies with long-baseline interferometry. Below, we first summarize the observations from each instrument and then describe the data reduction and analysis procedure. Table 1 lists observing parameters including dates, spectral band, spectral resolution, and integration time. It also lists the predicted flux ratio, separation, and relative RV at the time of observation based on the published orbits summarized above.

3.1. KPIC/VFN

The VFN observations are done following a similar procedure to that presented in previous KPIC papers (e.g., Wang et al. 2021). This involves: (1) observing an M giant to derive a wavelength solution, (2) observing an A0 standard star at a similar airmass as the target to sample the telluric transmission, (3) observing the primary star, and then (4) observing the companion. However, in contrast to the DS observations where we offset the fiber to the companion in step four, in VFN mode the primary star is kept on-axis but we insert a vortex mask so that it is nulled while the companion is preferentially coupled. Here, we summarize the KPIC data reduction procedure using the KPIC DRP (for details, see Wang et al. 2021). First, we remove the thermal background and persistent bad pixels from the raw images by using instrument background frames taken before the observing night. Then, we use data from the telluric standard star to fit the trace of each column in the KPIC science fibers and nine spectral orders, which give the position and standard deviation of the PSF in the spatial direction at each column. For every frame, we extracted the 1D spectra in each column of each spectral order. To remove residual background light, we subtracted the median of pixels that are at least 5 pixels away from every pixel in each column. Finally, we used optimal extraction (Horne 1986) to sum the flux using weights defined by the 1D Gaussian line-spread function profiles calculated from the spectra of the telluric star. We only use KPIC echelle order 6 ($\sim$2.29–2.34 μm—correspondingly NIRSPEC order 33) in this Letter since it covers the CO bandhead where we expect many strong absorption lines from the M dwarf companions. Furthermore, this echelle order is close to the central wavelength of 2.225 μm where the vortex provides the deepest nulls (Echeverri et al. 2023).

The data analysis procedure for VFN is nearly identical to that used for KPIC DS observations (e.g., Wang et al. 2021). In short, we build a forward model of the data from a linear combination of the residual primary star flux and the companion flux. We account for the telluric and instrumental response using the A0 star spectrum. To account for the residual light from the primary star, we use the empirical spectra from the on-axis DS observations taken in step three above. This assumes the companion signal is negligible compared to the primary star signal since the companion is significantly fainter and less efficiently coupled. For the companion model, we interpolate over a grid of BT-Settl (CIFIST) models (Allard et al. 2012), varying effective temperature ($T_{\rm eff}$) and surface gravity ($\log g$) while assuming solar metallicity. Additionally, we fit for the RV shift and projected rotational rate ($v \sin i$) of the companion. In KPIC data, a systematic fringing effect is introduced by Fabry–Perot cavities from transmissive optics in the instrument (Finnerty et al. 2022). To account for this fringing, we use the semiphysical fringing model described in Xuan et al. (2024) to model its effect on the data. This step is particularly important for VFN data since the characteristic fringing amplitude of $\sim$1%–3% (Xuan et al. 2024) caused by the residual primary starlight can be comparable to the companion signal in VFN observations. As a visual example of the elements that go into the forward model, Figure 1 shows the observed VFN mode spectrum for HIP 21543 along with the best-fit model and its various components. Furthermore, we carry out separate fits to DS mode (i.e., no nulling) spectra of the primary stars also using the BT-Settl models. The goal of these fits is to estimate the primary star's RV at the time of observation and calculate the relative RV, which we compare in Section 4 to the expected relative RVs from the published orbits. Note that unlike for the VFN data, where we fit a combination of primary and companion flux, we only need to account for a single stellar component when fitting the primary star spectra.

In addition to the spectral fits described above, we carry out a cross-correlation function (CCF) analysis to visualize the detection strength of the companion signal in our data (Figure 2). For the CCF analysis, we fix the companion

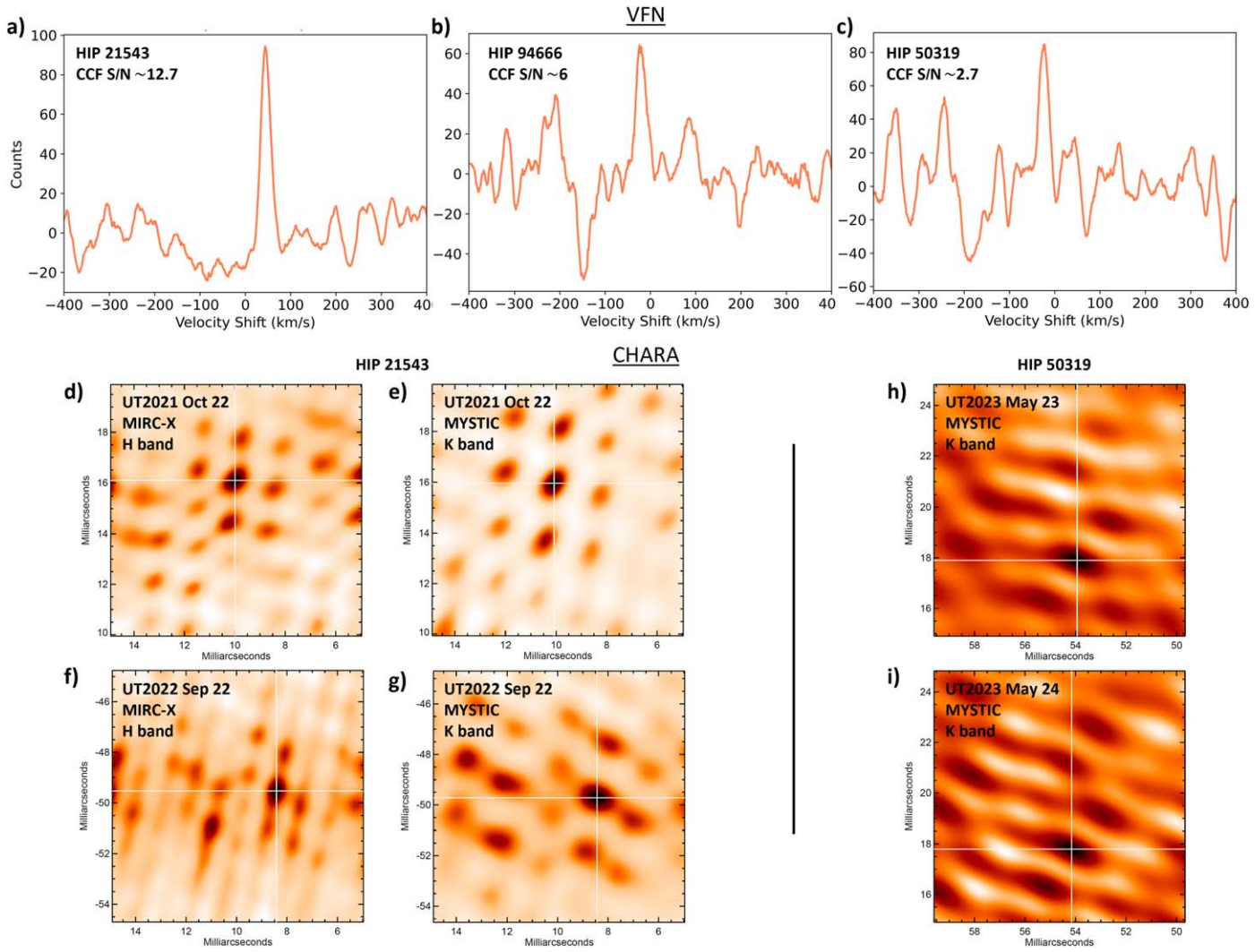

Figure 2. Top row: CCF between the best-fit model and the measured spectra for (a) HIP 21543, (b) HIP 94666, and (c) HIP 50319. The CCF S/N is included in the top left of the plots. The periodic oscillations in the CCF for HIP 50319 are due to residual fringing that was not fully removed in the fits, limiting us to a tentative detection on this target. Lower two rows: CHARA detection maps for HIP 21543 and HIP 50319. HIP 94666 is omitted as it was not detected by CHARA. The axes mark the distance in milliarcseconds from the primary, with north up and east left. The white crosshairs denote the detected companion. Four maps are shown for HIP 21543, two for MIRC-X ((d) and (f)) and two for MYSTIC ((e) and (g)), across both nights. HIP 50319 has two maps ((h) and (i)), both from MYSTIC, one for each night. The upper left text in the CHARA maps denotes the observing night, beam combiner, and band for each plot.

template to the best-fit model from the spectral fit. Then, we estimate the maximum likelihood value for both the companion flux and speckle flux in the data as a function of RV shift, following Ruffio et al. (2019) and Wang et al. (2021). The resulting estimate of the companion flux as a function of RV is the CCF. To estimate the signal-to-noise ratio (S/N) of the detection, we compare the peak in the CCF to the standard deviation of the wings out to $\pm 1000\,\mathrm{km\,s^{-1}}$; we report this value as the CCF S/N.

Though the VFN data provides spectra that constitute a detection on their own and can be used for characterization, they do not provide reliable flux ratio measurements. The derived $T_{\rm eff}$ for the companion could be used to estimate the companion luminosity but this would be highly model-dependent. Robustly constraining flux ratios would require photometric flux measurements that are contingent on knowing the throughput to the detector. With VFN, the fiber coupling efficiency, and hence throughput, for the companion light depends on the angular separation to the center of the fiber. However, VFN's single annular fringe does not provide any spatial information for the companion. This does not limit our detection capabilities but does prevent us from determining the observed flux from VFN observations alone. For these targets, we instead use CHARA to constrain the position and flux ratios directly.

3.2. CHARA/MIRC-X and MYSTIC

The Michigan InfraRed Combiner—eXeter (MIRC-X; Anugu et al. 2020) and the Michigan Young STar Imager (MYSTIC; Setterholm et al. 2023) on the Georgia State University Center for High Angular Resolution Astronomy (CHARA) Array (ten Brummelaar et al. 2005) were used to search for binary companions to all three targets. HIP 94666 and HIP 50319 were observed in 2023 specifically for a brief VFN follow-up program, with the latter target being observed over two nights. HIP 21543 had been observed twice in the past for other programs, so we used these archival data. The observations generally used all six 1 meter telescopes in the array, with baselines spanning 30–330 m, to provide an angular

Table 2
Fitted Parameters from VFN

Target (HIP)	MJD	Prim. RV (km s^{-1})	Comp. RV (km s^{-1})	Rel. RV (km s^{-1})	$T_{\rm eff}$ (K)	$v \sin i$ (km s^{-1})
21543	59864.52	$37.0^{+0.5}_{-0.6}$	$45.3^{+0.4}_{-0.5}$	$-8.3^{+0.6}_{-0.8}$	3480^{+90}_{-70}	$9.7^{+2.1}_{-0.9}$
94666	60073.62	$-10.2^{+0.2}_{-0.2}$	$-24.6^{+0.6}_{-0.5}$	$14.4^{+0.6}_{-0.5}$	4090^{+320}_{-230}	<7.2[a]
50319	60070.29	$-35.4^{+0.1}_{-0.1}$	$-17.2^{+0.9}_{-0.8}$	$-18.2^{+0.9}_{-0.8}$	3300^{+130}_{-140}	<10.1[a]

Note. MJD is the average value during the observation. Primary and companion RV values are with respect to the Earth–Sun barycenter using the barycentric RV correction from Table 1. $T_{\rm eff}$ and $v \sin i$ in this table are for the companion.
[a] Upper limit set at 2σ.

resolution down to $\frac{\lambda}{B_{\rm max}} \sim 1$ mas, although only five telescopes were available for the HIP 89010 observations. MIRC-X and MYSTIC were using their 6-beam All-in-One Combiners, providing up to 15 simultaneous baselines and 20 closure phases. Simultaneous MIRC-X and MYSTIC data were taken for each observation, with MIRC-X operating in the H band (1.50–1.72 μm) and MYSTIC in the K band (1.95–2.38 μm). Observing sequences involved interspersing target observations with calibrators to correct for the time-varying instrumental transfer function. See Table 1 for additional observing information.

We reduce the interferometric data with the public `mircx_pipeline` (Anugu et al. 2020) to produce raw visibilities and closure phases. We then calibrate the transfer function using the calibrator stars, estimating their size using `Search Cal` (Chelli et al. 2016). Then, we look for a binary companion using a simple grid search, fitting only to the closure phases, while fixing the diameter of the primary estimated from photometry (0.26 mas for HIP 21543 and 0.53 mas for HIP 50319; irrelevant for HIP 94666 due to nondetection with CHARA). We note that closure phases are based on the sum of phases around closed triangles of baselines and are relatively free from calibration systematics that affect the visibility amplitudes (Monnier 2007). MIRC-X and MYSTIC each had different spectral resolutions and thus different interferometric fields of view and contrast sensitivities. Coupled with varying seeing conditions and different total observing times, there are some nights for which we are unable to recover reliable companion detections with both instruments. For the results reported below, we have applied the final wavelength correction terms found in Torres et al. (2022). With such a limited "pilot program" data set, our error analysis is simplified, estimating position errors using the shape of the chi-squared surface immediately surrounding the best-fit companion position (see Figure 2), while upper limits on contrasts are derived from the contrast ratios from the best-fitting noise peaks.

4. Results and Discussion

The VFN observations yielded confident detections on two of the companions while the third, HIP 50319 B, gave a tentative detection. Meanwhile, the CHARA observations yielded two confident detections and one nondetection, HIP 94666 Ab. Using the extracted KPIC spectra, we make a first pass here at characterizing the companions to showcase the science capabilities of VFN, especially when combined with the input from CHARA. Tables 2 and 3 summarize the best-fit values derived from the VFN and CHARA observations, respectively. The VFN fits fail to properly constrain $\log g$ for the companions, which is partly due to the relatively low S/N and small wavelength coverage used for this VFN demonstration ($\sim$2.29–2.34 μm). In addition, constraining fundamental properties of M dwarfs, such as $\log g$ and $T_{\rm eff}$, is a challenging task and still remains somewhat model-dependent (e.g., Rajpurohit et al. 2018). For example, the atmospheric models used to estimate $T_{\rm eff}$ and $\log g$ may include inaccurate opacity data from outdated line lists and insufficient treatment of dust opacity in late-type M dwarfs (Iyer et al. 2023; Sanghi et al. 2023). Furthermore, the BT-Settl grid we use has a coarse grid spacing of 0.5 dex in $\log g$, which could introduce interpolation issues (Zhang et al. 2021). Despite these challenges, our derived $T_{\rm eff}$ for two of the targets was close to the expected value, and only the HIP 94666 Ab temperature seems to significantly deviate from expectation, as explained below. Thus, the VFN data provide the first spectra for the companions and the first constraints on their RV, $v \sin i$, and $T_{\rm eff}$. Given the high amplitude of residual primary flux in VFN spectra, the fringing signal is strong and remains the dominant source of error in our spectral fits. Beyond the VFN results, the CHARA results provide the first flux ratio and direct position measurements for the companions.

HIP 21543 shows a strong detection with both instruments. Figure 1 shows the VFN mode spectrum, the best-fit full model, the on-axis DS mode spectrum used as the contribution from the primary in the model, and the resulting best-fit companion spectrum. The CCF between the best-fit model and the VFN data is shown in Figure 2(a), yielding a CCF S/N of 12.7. The best-fit spectrum for the companion clearly shows two CO bandheads at around 2.295 and 2.322 μm. From this spectrum, we measure a companion RV of $37.0^{+0.5}_{-0.6}$ km s^{-1}. The fits to the DS mode spectra (not shown) give a primary RV of $45.3^{+0.4}_{-0.5}$ km s^{-1}. This yields a relative RV of $-8.3^{+0.6}_{-0.8}$ km s^{-1} between the primary and the companion on UT 2022 October 12, which agrees with the expected value of -7.9 km s^{-1} from the Tokovinin orbit and is close to the -6.9 km s^{-1} from the Gaia orbit. The best-fit $T_{\rm eff}$ just over 3450 K for Ab is slightly higher than, though still consistent with, the expected 3200–3300 K from the MSDT given the mass estimates. CHARA detected Ab with both MIRC-X and MYSTIC on both nights, as shown in Figures 2(d)–(g). The resulting separations of 18.9 mas and 50.3 mas for the two epochs are consistent with the expected values from both the Tokovinin orbit (20.5 and 47.3 mas) and the Gaia orbit (22.0 and 52.8 mas). The CHARA data also yield a K-band flux ratio from MYSTIC of 70 ± 11 between Ab and Aa, which is between the expected flux ratios of 42 and 85, again from the Tokovinin and Gaia masses, respectively.

HIP 94666 has a confident detection in the KPIC VFN data with a CCF S/N of 6 as shown in Figure 2(b). Constraining the

Table 3
Fitted Parameters from CHARA

Target (HIP)	MJD	Instrument	Flux Ratio	Obs. Band	Sep. (mas)	PA (E of N)	Error Ellipse		
							Major Ax. (mas)	Minor Ax. (mas)	PA of Major Ax. (deg)
21543	59509.323	MIRC-X	73	*H*	18.95	31.83	0.15	0.10	313
21543	59509.323	MYSTIC	59	*K*	18.88	32.28	0.10	0.07	326
21543	59844.485	MIRC-X	75	*H*	50.24	170.35	0.12	0.08	344
21543	59844.485	MYSTIC	81	*K*	50.43	170.37	0.70	0.50	66
94666	60079.470	MIRC-X	>70	*H*	…	…	…	…	…
94666	60079.470	MYSTIC	>40	*K*	…	…	…	…	…
50319	60087.201	MIRC-X	>180	*H*	…	…	…	…	…
50319	60087.201	MYSTIC	407	*K*	56.83	71.64	0.26	0.11	69
50319	60088.201	MIRC-X	>200	*H*	…	…	…	…	…
50319	60088.201	MYSTIC	451	*K*	57.00	71.81	0.69	0.31	65

$T_{\rm eff}$ proved most challenging for this target out of the three. Our fits give 4090^{+320}_{-230} *K*, which is 800 K higher than the expected $T_{\rm eff} \sim 3250$ K from the Gaia-derived companion mass of $\sim 0.24\,M_{\odot}$. Part of the discrepancy could be due to underestimation in the Gaia mass ratio (and thereby flux ratio), for example, if the secondary is bright enough to cause line blending (Tokovinin 2023). However, the CHARA nondetection puts a lower limit to the flux ratio of >40 in the *K* band, so line blending might be unlikely. On the other hand, our derived $T_{\rm eff}$ from the BT-Settl atmospheric models may be incorrect, as commonly seen in previous works on late M dwarfs (Sanghi et al. 2023; Xuan et al. 2024). For early M dwarfs like HIP 94666 Ab, however, $T_{\rm eff}$ accuracies of 100 K or lower have been achieved (e.g., Neves et al. 2014; Cristofari et al. 2022), which may indicate that our fits are being biased by residual fringing from the bright primary star. Despite the challenges with the $T_{\rm eff}$, our relative RV of $14.4^{+0.6}_{-0.5}$ km s^{-1} on 2023 May 9 is close to the predicted value of 13.5 km s^{-1} from the Gaia orbital solution. The CHARA observation yielded unreliable values in the short amount of integration time provided, such that we cannot provide position values and can only set lower limits on the flux ratio for the companion. We plan to reobserve this target with CHARA in 2024, which could inform of the true flux ratio and help resolve our discrepancy on the temperature.

HIP 50319 yielded a tentative VFN detection, with a CCF S/N of 2.7. The CCF, shown in Figure 2(c), has a prominent structure in the wings, reflecting the fact that the detection is primarily limited by residual fringing. However, the best-fit model provides several pieces of evidence supporting the validity of this detection. First, the best-fit RV of -35.4 ± 0.1 km s^{-1} for the primary on 2023 May 6 is in line with the published velocity of ~ -34 km s^{-1} (Deka-Szymankiewicz et al. 2018; Nordström et al. 2004). Our fit to the primary further gives a $T_{\rm eff}$ of 5480 ± 10 K and $v \sin i$ of 3.9 ± 0.2 km s^{-1}, which are close to the published values of 5686 ± 7 K (Deka-Szymankiewicz et al. 2018) and 5.5 km s^{-1} (Luck 2017). Meanwhile, the fits to the companion spectrum show an RV of $-17.2^{+0.9}_{-0.8}$ km s^{-1} with a $T_{\rm eff} \approx 3300$ K. This $T_{\rm eff}$ is close to the expected value of around 3000 K from the MSDT given the estimated mass. The fact that the retrieved properties for the primary are in line with prior measurements, and that the companion RV and $T_{\rm eff}$ are so different, provide strong evidence that our analysis of the VFN mode spectra is indeed detecting spectral lines from two distinct objects.

The VFN-measured relative RV of $-18.2^{+0.9}_{-0.8}$ km s^{-1} is 2 times larger than expected from the Gaia orbital solution, which predicts a relative RV of -9.2 ± 3.0 km s^{-1} at the time of the KPIC observations. It is possible that our VFN relative RVs for this system are biased by residual fringing in the data. Acquiring higher S/N spectra without fringing (see Section 5) could help confirm this. Alternatively, the Gaia orbit may not be entirely accurate. The CHARA MYSTIC observations, shown in Figures 2(h) and (i), yielded confident detections that put the companion at a separation of around 56.9 ± 0.3 mas for the two consecutive nights. This is 1σ higher than the Gaia-predicted separation of 42 ± 14 mas for the CHARA observation epoch, supporting a possible error in the Gaia orbital solution. Similar discrepancies between ground-based RVs and Gaia NSS orbital solutions have been found in other studies (Winn 2022; Tokovinin 2023), and have been attributed to incorrect orbital inclinations (Marcussen & Albrecht 2023). However, the exact cause of the issue is unclear since only orbital solutions, and not the time-series astrometry, are published in Gaia DR3. The CHARA MYSTIC detections provide a *K*-band flux ratio of 429 ± 22, which agrees with the predicted value of 405 presented in Section 2, implying that the Gaia mass ratio and companion mass of $0.11 M_{\odot}$ is likely accurate. The MIRC-X data were unable to constrain the separation and only provided lower limits for the *H*-band flux ratio.

Thus, the CHARA MYSTIC detection confirms that the companion was within the VFN field of view and should have been detectable at the time of observation. It also shows that the published orbital solution likely has errors that could explain the larger-than-expected relative RV from VFN. This, combined with the measured $T_{\rm eff}$ of the primary and companion, suggests a promising KPIC VFN detection of HIP 50319 B.

5. Conclusion

In this Letter, we presented the first direct detections of three close-in low-mass stellar companions previously only known through indirect methods. The first two targets were confidently detected by VFN with CCF S/Ns of 6 and 12.7. Meanwhile, for the most challenging target, our VFN detection is tentative due to strong fringing, which could not be fully fitted and removed. An upgrade to KPIC in 2024 February will replace the optics that introduce fringing, significantly reducing the effect of this error in future observations. We will also add a

new vortex mask, which will further improve the S/N by doubling the off-axis throughput and pushing the peak coupling from 1.4 λ/D to 0.9 λ/D. Nevertheless, the current performance is sufficient for detection and characterization, as we are able to retrieve effective temperatures, rotational velocities, and RV values for the companions that are generally consistent with expectations. These VFN detections were made at separations between 35 and 55 mas, corresponding to around 0.7–1.2 λ/D and about 2 au. That is well within the typical IWA of conventional coronagraphs at these wavelengths, highlighting the power of cross-aperture nulling.

Previous single-telescope interferometric techniques have generally shown on-sky contrast limits of ∼1500 at $\lesssim$2.5 λ/D (Gauchet et al. 2016; Sallum & Skemer 2019), leading to demonstrated companion detections at flux ratios of a few hundred within 2 λ/D (Hinkley et al. 2015; Lloyd et al. 2006; Biller et al. 2012). A prior cross-aperture fiber nuller detected η Peg B with a flux ratio of 100 and measured the stellar diameter of the primary at a flux ratio of ∼2000 (Serabyn et al. 2019). Our previous VFN paper predicted contrast limits of ∼1000 at ∼1 λ/D (Echeverri et al. 2023), and this Letter now adds companion detections with flux ratios around 100 and a tentative detection at ∼430. These VFN results also represent the first companion detection at these contrast levels with high ($R > 10{,}000$) spectral-resolution nulling on-sky, showcasing the power of combining nulling interferometry with high-resolution spectroscopy and complementing the capabilities of previous instruments. In addition, these results are obtained at or within the conventional diffraction limit.

To validate our VFN detections with a well-established technique, this Letter combined KPIC VFN results with observations from CHARA. CHARA had confident detections on two of the targets, including the most challenging one that was tentative for VFN. This allowed us to verify that we are close to our VFN contrast predictions from Echeverri et al. (2023). Moreover, our combined results highlight the complementary nature between long-baseline interferometry and cross-aperture nulling techniques. For example, the CHARA-provided positions substantiate the published orbits, especially when combined with relative RV values from KPIC VFN. We find that the published orbits for the first two targets, HIP 21543 Ab and HIP 94666 Ab, are consistent with our results, while the orbit for the third, HIP 50319 B, likely needs to be updated. These results open the door to detecting faint companions around young stars at separations within the IWA of typical coronagraphic imagers. Finally, they also point to an observing scheme that leverages the individual capabilities of VFN and CHARA. Future surveys with CHARA and VFN can target young stars with Gaia–Hipparcos astrometric accelerations indicative of substellar companions. These interferometric surveys would complement imaging surveys already underway (e.g., Currie et al. 2021; Kuzuhara et al. 2022; De Rosa et al. 2023) to provide astrometric, flux ratio, and high-resolution spectral measurements at smaller separations, for a more efficient and complete view of faint, close-in companions.

Acknowledgments

D.E. was supported by a NASA Future Investigators in NASA Earth and Space Science and Technology (FINESST) fellowship under award #80NSSC19K1423. D.E. also acknowledges support from the Keck Visiting Scholars Program (KVSP) to install the KPIC Phase II upgrades required for KPIC VFN. J.X. is supported by another FINESST award under #80NSSC23K1434 and also acknowledges support from the KVSP to commission KPIC Phase II.

Funding for KPIC has been provided by the California Institute of Technology, the Jet Propulsion Laboratory, the Heising-Simons Foundation (grants #2015-129, #2017-318, #2019-1312, and #2023-4598), the Simons Foundation (through the Caltech Center for Comparative Planetary Evolution), and the NSF under grant AST-1611623.

This work is based upon observations obtained with the Georgia State University Center for High Angular Resolution Astronomy Array at Mount Wilson Observatory. The CHARA Array is supported by the National Science Foundation under grant Nos. AST-1636624 and AST-2034336. Institutional support has been provided from the GSU College of Arts and Sciences and the GSU Office of the Vice President for Research and Economic Development. S.K. and S.C. acknowledge funding for MIRC-X received from the European Research Council (ERC) under the European Union's Horizon 2020 research and innovation programme (starting grant No. 639889 and consolidated grant No. 101003096). J.D.M. acknowledges funding for the development of MIRC-X (NASA-XRP NNX16AD43G, NSF-AST 1909165) and MYSTIC (NSF-ATI 1506540, NSF-AST 1909165).

The data presented herein were obtained at Keck Observatory, which is a private 501(c)3 nonprofit organization operated as a scientific partnership among the California Institute of Technology, the University of California, and the National Aeronautics and Space Administration. The Observatory was made possible by the generous financial support of the W. M. Keck Foundation.

Some of this work was carried out at the Jet Propulsion Laboratory, California Institute of Technology, under contract with the National Aeronautics and Space Administration and funded through the internal Research and Technology Development program.

This work has made use of data from the European Space Agency (ESA) mission Gaia (https://www.cosmos.esa.int/gaia), processed by the Gaia Data Processing and Analysis Consortium (DPAC; https://www.cosmos.esa.int/web/gaia/dpac/consortium). Funding for the DPAC has been provided by national institutions, in particular, the institutions participating in the Gaia Multilateral Agreement.

The authors wish to recognize and acknowledge the very significant cultural role and reverence that the summit of Maunakea has always had within the indigenous Hawaiian community. We are most fortunate to have the opportunity to conduct observations from this mountain.

Facilities: Keck:II (KPIC), CHARA (MIRC-X/MYSTIC).

Software: KPIC DRP (https://github.com/kpicteam/kpic_pipeline), mircx_pipeline (https://gitlab.chara.gsu.edu/lebouquj/mircx_pipeline), Search Cal (https://www.jmmc.fr/english/tools/proposal-preparation/search-cal/), Astropy (https://www.astropy.org/index.html; Astropy Collaboration et al. 2022, 2018, 2013).

ORCID iDs

Daniel Echeverri https://orcid.org/0000-0002-1583-2040
Jerry W. Xuan https://orcid.org/0000-0002-6618-1137
John D. Monnier https://orcid.org/0000-0002-3380-3307
Jacques-Robert Delorme https://orcid.org/0000-0001-8953-1008
Jason J. Wang https://orcid.org/0000-0003-0774-6502

Nemanja Jovanovic https://orcid.org/0000-0001-5213-6207
Katelyn Horstman https://orcid.org/0000-0001-9708-8667
Garreth Ruane https://orcid.org/0000-0003-4769-1665
Bertrand Mennesson https://orcid.org/0000-0003-4205-4800
Dimitri Mawet https://orcid.org/0000-0002-8895-4735
J. Kent Wallace https://orcid.org/0000-0001-5299-6899
Ashley Baker https://orcid.org/0000-0002-6525-7013
Benjamin Calvin https://orcid.org/0000-0003-4737-5486
Luke Finnerty https://orcid.org/0000-0002-1392-0768
Michael P. Fitzgerald https://orcid.org/0000-0002-0176-8973
Chih-Chun Hsu https://orcid.org/0000-0002-5370-7494
Joshua Liberman https://orcid.org/0000-0002-4934-3042
Maxwell Millar-Blanchaer https://orcid.org/0000-0001-6205-9233
Evan Morris https://orcid.org/0000-0003-3165-0922
Jean-Baptiste Ruffio https://orcid.org/0000-0003-2233-4821
Ben Sappey https://orcid.org/0000-0003-1399-3593
Andrew J. Skemer https://orcid.org/0000-0001-6098-3924
Ji Wang https://orcid.org/0000-0002-4361-8885
Yinzi Xin https://orcid.org/0000-0002-6171-9081
Narsireddy Anugu https://orcid.org/0000-0002-2208-6541
Sorabh Chhabra https://orcid.org/0000-0001-8926-9732
Noura Ibrahim https://orcid.org/0000-0002-1788-9366
Stefan Kraus https://orcid.org/0000-0001-6017-8773
Gail H. Schaefer https://orcid.org/0000-0001-5415-9189
Cyprien Lanthermann https://orcid.org/0000-0001-9745-5834

References

Allard, F., Homeier, D., & Freytag, B. 2012, RSPTA, 370, 2765
Anugu, N., Le Bouquin, J.-B., Monnier, J. D., et al. 2020, AJ, 160, 158
Astropy Collaboration, Robitaille, T. P., Tollerud, E. J., et al. 2013, A&A, 558, A33
Astropy Collaboration, Price-Whelan, A. M., Sipőcz, B. M., et al. 2018, AJ, 156, 123
Astropy Collaboration, Price-Whelan, A. M., Lim, P. L., et al. 2022, ApJ, 935, 167
Beijersbergen, M. W., Coerwinkel, R. P. C., Kristensen, M., & Woerdman, J. P. 1994, OptCo, 112, 321
Bender, C. F., & Simon, M. 2008, ApJ, 689, 416
Beuzit, J. L., Vigan, A., Mouillet, D., et al. 2019, A&A, 631, A155
Biller, B., Lacour, S., Juhász, A., et al. 2012, ApJL, 753, L38
Chelli, A., Duvert, G., Bourgès, L., et al. 2016, A&A, 589, A112
Cristofari, P. I., Donati, J. F., Masseron, T., et al. 2022, MNRAS, 511, 1893
Currie, T., Brandt, T. D., Kuzuhara, M., et al. 2021, Proc. SPIE, 11823, 1182304
De Furio, M., Gardner, T., Monnier, J., et al. 2022, ApJ, 941, 118
De Rosa, R. J., Nielsen, E. L., Wahhaj, Z., et al. 2023, A&A, 672, A94
Deka-Szymankiewicz, B., Niedzielski, A., Adamczyk, M., et al. 2018, A&A, 615, A31
Delorme, J.-R., Jovanovic, N., Echeverri, D., et al. 2021, JATIS, 7, 035006
Echeverri, D., Ruane, G., Jovanovic, N., Mawet, D., & Levraud, N. 2019, OptL, 44, 2204
Echeverri, D., Ruane, G., Jovanovic, N., et al. 2021, Proc. SPIE, 11823, 118230A
Echeverri, D., Jovanovic, N., Delorme, J.-R., et al. 2022, Proc. SPIE, 12184, 121841W
Echeverri, D., Xuan, J., Jovanovic, N., et al. 2023, JATIS, 9, 035002
Finnerty, L., Schofield, T., Delorme, J.-R., et al. 2022, Proc. SPIE, 12184, 121844Y
Finnerty, L., Schofield, T., Sappey, B., et al. 2023, AJ, 166, 31
Fulton, B. J., Rosenthal, L. J., Hirsch, L. A., et al. 2021, ApJS, 255, 14
Gaia Collaboration, Arenou, F., Babusiaux, C., et al. 2023, A&A, 674, A34
Gauchet, L., Lacour, S., Lagrange, A. M., et al. 2016, A&A, 595, A31
Griffin, R. F., Gunn, J. E., Zimmerman, B. A., & Griffin, R. E. M. 1988, AJ, 96, 172
Hinkley, S., Kraus, A. L., Ireland, M. J., et al. 2015, ApJL, 806, L9
Holl, B., Sozzetti, A., Sahlmann, J., et al. 2023, A&A, 674, A10
Horne, K. 1986, PASP, 98, 609
Iyer, A. R., Line, M. R., Muirhead, P. S., Fortney, J. J., & Gharib-Nezhad, E. 2023, ApJ, 944, 41
Kuzuhara, M., Currie, T., Takarada, T., et al. 2022, ApJL, 934, L18
Lanthermann, C., Le Bouquin, J. B., Sana, H., et al. 2023, A&A, 672, A6
Lloyd, J. P., Martinache, F., Ireland, M. J., et al. 2006, ApJL, 650, L131
Lockwood, G. W., Thompson, D. T., Radick, R. R., et al. 1984, PASP, 96, 714
Luck, R. E. 2017, AJ, 153, 21
Macintosh, B., Graham, J. R., Ingraham, P., et al. 2014, PNAS, 111, 12661
Marcussen, M. L., & Albrecht, S. H. 2023, AJ, 165, 266
Mason, B. D., McAlister, H. A., Hartkopf, W. I., & Bagnuolo, W. G. J. 1993, AJ, 105, 220
Mawet, D. 2021, NatAs, 5, 723
Monnier, J. D. 2007, NewAR, 51, 604
Neves, V., Bonfils, X., Santos, N. C., et al. 2014, A&A, 568, A121
Nordström, B., Mayor, M., Andersen, J., et al. 2004, A&A, 418, 989
Pecaut, M. J., & Mamajek, E. E. 2013, ApJS, 208, 9
Rajpurohit, A. S., Allard, F., Teixeira, G. D., et al. 2018, A&A, 610, A19
Riddle, R. L., Tokovinin, A., Mason, B. D., et al. 2015, ApJ, 799, 4
Roberts, L. C. J., Tokovinin, A., Mason, B. D., & Marinan, A. D. 2017, AJ, 153, 100
Roettenbacher, R. M., Monnier, J. D., Fekel, F. C., et al. 2015a, ApJ, 809, 159
Roettenbacher, R. M., Monnier, J. D., Henry, G. W., et al. 2015b, ApJ, 807, 23
Rosenthal, L. J., Fulton, B. J., Hirsch, L. A., et al. 2021, ApJS, 255, 8
Ruane, G., Echeverri, D., Jovanovic, N., et al. 2019, Proc. SPIE, 11117, 1111716
Ruane, G., Wang, J., Mawet, D., et al. 2018, ApJ, 867, 143
Ruffio, J.-B., Macintosh, B., Konopacky, Q. M., et al. 2019, AJ, 158, 200
Ruffio, J.-B., Horstman, K., Mawet, D., et al. 2023, AJ, 165, 113
Sallum, S., & Skemer, A. 2019, JATIS, 5, 018001
Sanghi, A., Liu, M. C., Best, W. M. J., et al. 2023, ApJ, 959, 63
Serabyn, E., Mennesson, B., Martin, S., Liewer, K., & Kühn, J. 2019, MNRAS, 489, 1291
Setterholm, B. R., Monnier, J. D., Le Bouquin, J.-B., et al. 2023, JATIS, 9, 025006
ten Brummelaar, T. A., McAlister, H. A., Ridgway, S. T., et al. 2005, ApJ, 628, 453
Thomas, J. D., Richardson, N. D., Eldridge, J. J., et al. 2021, MNRAS, 504, 5221
Tokovinin, A. 2014, AJ, 147, 87
Tokovinin, A. 2018, ApJS, 235, 6
Tokovinin, A. 2021, AJ, 161, 144
Tokovinin, A. 2023, AJ, 165, 220
Torres, G., Schaefer, G. H., Monnier, J. D., et al. 2022, ApJ, 941, 8
Wang, J., Kolecki, J. R., Ruffio, J.-B., et al. 2022, AJ, 163, 189
Wang, J., Wang, J. J., Ruffio, J.-B., et al. 2023, AJ, 165, 4
Wang, J. J., Ruffio, J.-B., Morris, E., et al. 2021, AJ, 162, 148
Winn, J. N. 2022, AJ, 164, 196
Xuan, J. W., Wang, J., Ruffio, J.-B., et al. 2022, ApJ, 937, 54
Xuan, J. W., Wang, J., Finnerty, L., et al. 2024, ApJ, 962, 10
Zhang, Z., Liu, M. C., Marley, M. S., Line, M. R., & Best, W. M. J. 2021, ApJ, 916, 53